Starlight Pointing Subsystem for the Formation Interferometer Testbed (FIT)

Joel Shields, Sam Sirlin, Matt Wette
Jet Propulsion Laboratory
4800 Oak Grove Drive
Pasadena CA 91109-8099
818-354-5050
Joel.F.Shields@jpl.nasa.gov

Abstract— StarLight is a NASA\JPL sponsored mission that will be the first spaceborn stellar interferometer. The objective of the mission is to develop and test technologies for performing interferometric observations in space and for the extremely precise formation flying required to make the instrument work. The Formation Interferometer Testbed (FIT) is a ground based prototype of the two spacecraft StarLight instrument.

In this paper a complete model of the FIT pointing system is characterized that includes backlash in the siderostat (SD), hysteresis in the PZT actuators of the fast steering mirrors (FSM), time delays, and air path disturbances. Based on this model, a dual stage pointing controller is designed that achieves a bandwidth sufficient to satisfy the pointing requirement. Simulated and experimental results are given that validate the performance of the pointing system.

TABLE OF CONTENTS

1. INTRODUCTION

The Formation Interferometer Testbed (FIT) is a ground based prototype of the instrument aboard the two spacecraft StarLight mission. StarLight is a New Millennium technology mission designed to demonstrate space based optical interferometry and the precision formation flying required for instrument operations. As depicted in Figure 1 light from a single source is collected from two separated spacecraft and combined at a central location to form interference patterns referred to as fringes. Detection of fringes allows for precise astrometric measurements. Key to this process of fringe detection is angular alignment of the wavefronts at each of the separated apertures. The wavefront tilt in each aperture is sensed on the combiner spacecraft by a CCD camera configured as an angle sensor. Three siderostats, two aboard the combiner spacecraft and one aboard the collector spacecraft are used to null the error signal from this sensor.

0-7803-5846-5/00/ 10.00 ©2002 IEEE

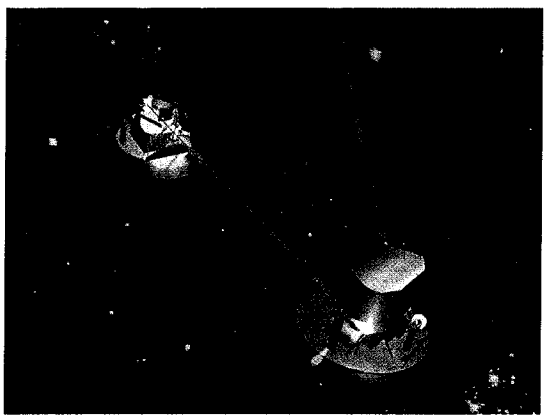

Figure 1. The StarLight mission ... the first ever formation flying stellar interferometer. Combiner spacecraft is shown in the near field, collector spacecraft is shown in the far field.

The FIT testbed is comprised of three main optical benches. The pseudostar bench functions as both a metrology and white light source. The collector bench is used to mimic the collector spacecraft. To simulate relative motion between the two spacecraft in a zero g environment, the optics on the collector bench can be moved in 6 DOF using a Hexapod (PI M-850). The combiner bench, depicted in Figure 2, collects light from both the pseudostar and collector and exposes the combined light onto a CCD camera (Collins EEV, 40X40 pixels, 24 microns per pixel). The focal plane of the camera is shown in Figure 2. Light from an inner annulus of each compressed (4X) stellar beam is overlapped and used to detect the interference fringes. Light from the outer annulus of the stellar beam is separated from the fringe light and used as a proxy to sense motion of the fringe spots. By stabilizing the motion of both pointing spots, the wavefronts at the fringe spots are guaranteed to be aligned.

The unique aspect of the FIT testbed relative to other interferometry testbeds at JPL is the ability to mimic relative motion between the collector and combiner spacecraft. To compensate for this motion, and other disturbances, the FIT testbed is equipped with a sophisticated pointing system comprised of one metrology pointing control system and two stellar pointing control loops. Each stellar loop has both coarse motion siderostats and fine motion fast steering

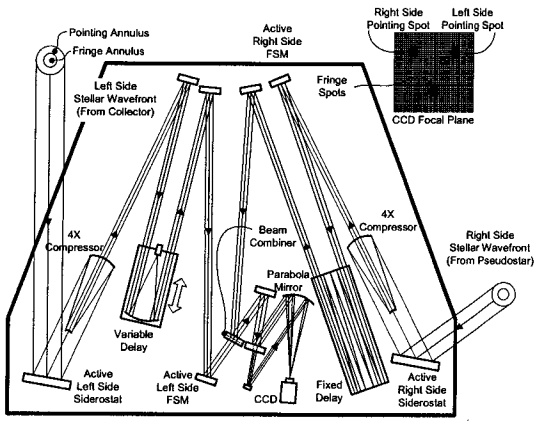

Figure 2. Overhead schematic of the combiner optical bench.

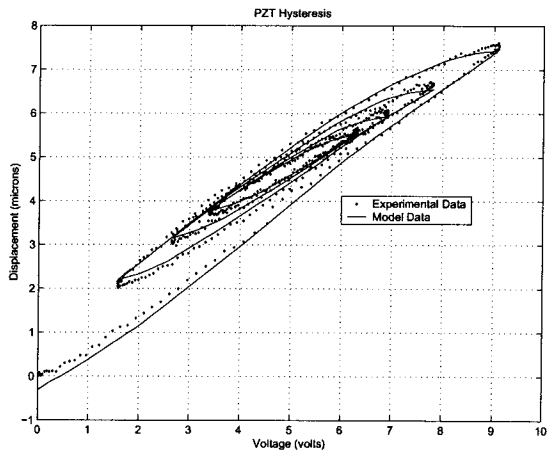

Figure 3. Experimental and modelled hysteresis behavior. Response to an underdamped step voltage command.

mirrors as active components. The metrology loop uses an array of photodiodes recessed into a transfer mirror on the collector bench to detect the position of a metrology laser launched from the combiner bench. The position of this beam is controlled using the siderostat on the left side of the combiner. The metrology loop is described in detail in a companion paper [1]. This paper focuses on the stellar loops, and in particular, the stellar loop on the right side of the instrument.

In section 2 a detailed model of the pointing system is developed. This model includes actuator dynamics and nonlinearities, disturbance sources, and delays. Section 3 describes the controller design for both the coarse and fine actuators. Section 4 presents simulation and experimental results that confirm the proper operation of the pointing system. Conclusions and recommendations are given in section 5.

2. Pointing System Characterization

High performance control design relies on accurate modelling of the system. Embedding knowledge of the system in the controller is ultimately the only way to maximize stability margins and performance. In this section, a detailed model of the stellar pointing system is developed for the purposes of controller design and performance prediction. The functional components of the right side pointing system are the large aperture siderostat, 4X compressor, small aperture fast steering mirror, parabolic mirror (Focal length 0.457 meters.), and CCD camera. The model accounts for the effect of each of these elements on the stellar wavefront.

The pointing requirement for each side of the FIT interferometer is to stabilize the stellar wavefront, in tip and tilt, to within 0.25 arc seconds RMS on the sky. In terms of pixel accuracy, this corresponds to one tenth of a pixel in either axis of the focal plane. Although the encoders on each axis of the large aperture siderostats have a resolution of 12.5 milli-arc seconds, backlash in the drive mechanism of the mirror gimbals reduces this accuracy to approximately 1.0 arc seconds [1]. As a result, the pointing accuracy of the siderostat at the focal plane is on the order of 0.37 pixels, not enough to meet the pointing specification. To improve the pointing capability of the instrument, while retaining the large field of regard provided by the siderostats, small aperture fast steering mirrors were added to the optical path of the stellar light. A description of each of these elements follows.

Coarse Siderostat

The siderostats used in the FIT testbed are Aerotech AOM130-6M gimbal mounts. The mount is actuated in azimuth and elevation with two BM75E brushless servo motors and two BAL 20-40-A linear servo amplifiers. The amplifiers were configured to operate in velocity mode to reduce the influence of friction. The mount is indirect drive using a spur gear and ball screw type arrangement to effect motion of the mirror mount. 4000 line encoders, after quadrature, are mounted at the motor shaft to sense the position of the mount. Using the encoders for feedback, a 40-50 Hz bandwidth position servo was designed and used as an intermediate servo for the stellar loop.

The backlash in the drive of the siderostat was characterized using the encoder and angular metrology sensor configured to directly measure the mirror orientation [1].

Fast Steering Mirror

The small aperture fast steering mirrors steer the starlight after the 4X-compressor. Functionally, these mirrors work in parallel with the coarse siderostat. Each FSM is articulated with a piezo-electric kinematic mount (Thorlabs KC1-PZ) consisting of three 8.0 micron stroke PZT stacks (Part number AE0505D08) which provide ±36.5 arc seconds tip\tilt angular range. Each PZT is commanded using

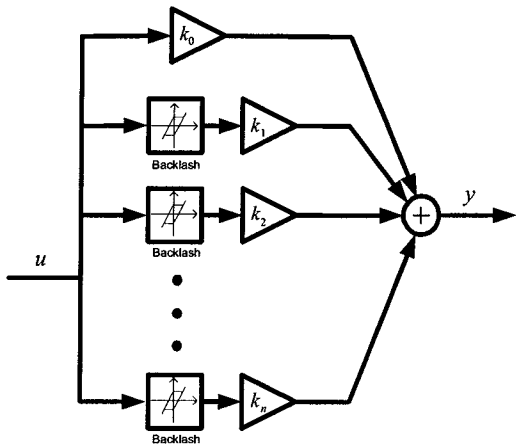

Figure 4. Model for hysteresis composed of parallel connection of backlash elements. Each element has a unique deadzone and output gain.

a 0-10 volt 16 bit D\A channel. Drive electronics (Thorlabs MDT693-EC) amplify this signal before it is applied to the PZT stack. The PZT elements are arranged on three corners of the square mount so that to move the mirror surface in azimuth and elevation one would apply the following voltages,

$$\begin{bmatrix} V_1 \\ V_2 \\ V_3 \end{bmatrix} = \frac{1}{SF_{PZT}} \underbrace{\begin{bmatrix} r & r \\ r & -r \\ -r & -r \end{bmatrix}}_{\mathbf{S}} \begin{bmatrix} \phi^{FSM}_{des.Az.} \\ \phi^{FSM}_{des.El.} \end{bmatrix} + \begin{bmatrix} V_{bias} \\ V_{bias} \\ V_{bias} \end{bmatrix} \quad (1)$$

where $\phi^{FSM}_{des.Az.}$ and $\phi^{FSM}_{des.El.}$ are the desired azimuth and elevation angles, SF_{PZT} is the linear scale factor between the applied voltage and PZT displacement, and r is the radius from the center of the mirror to the PZT stacks. Note that this equation assumes that each of the PZT stacks have been biased to their mid stroke position with a bias voltage, V_{bias}, of 5 volts. Equation (1) is designed to eliminate piston motion of the mirror. The piston motion of the mirror is undesirable since it introduces a disturbance into the instrument's path length control system.

If the PZT displacements were an exact linear relationship with the applied voltage, using Equation (1) to calculate the command voltages would accomplish zero piston motion. Unfortunately, this is not the case, as the PZT stacks have a significant amount of hysteresis. As a result, we can expect the mirrors to have some parasitic piston motion which can be calculated, a priori, from the PZT displacements. To perform this calculation, we first define an inertial coordinate system with its origin coincident to the center of the mirror surface, the x-axis along the mirror surface parallel to the optical bench, the y-axis along the mirror surface perpendicular to the optical bench, and the z-axis normal to the mirror surface pointing in the direction of reflected light rays. In this coordinate system, we can define the following vectors which represent the effective PZT actuation points on the mirror surface.

$$\mathbf{v_1} = \begin{pmatrix} -r \\ r \\ s_1 - \frac{s_{max}}{2} \end{pmatrix} \quad \mathbf{v_2} = \begin{pmatrix} -r \\ -r \\ s_2 - \frac{s_{max}}{2} \end{pmatrix} \quad \mathbf{v_3} = \begin{pmatrix} r \\ -r \\ s_3 - \frac{s_{max}}{2} \end{pmatrix} \quad (2)$$

where, s_1, s_2, and s_3 are the PZT elongations and s_{max} is the maximum elongation. The mirror normal can be calculated from these vectors by,

$$\mathbf{n_{FSM}} = \frac{(\mathbf{v_3} - \mathbf{v_2}) \times (\mathbf{v_1} - \mathbf{v_2})}{\| (\mathbf{v_3} - \mathbf{v_2}) \times (\mathbf{v_1} - \mathbf{v_2}) \|_2}. \quad (3)$$

Combining Equations (2) and (3) the amount of piston motion can be found using,

$$\alpha = \frac{\mathbf{n^T_{FSM}} \mathbf{v_3}}{\mathbf{n^T_{FSM}} \hat{\mathbf{z}}}, \quad (4)$$

where $\hat{\mathbf{z}} = [0\ 0\ 1]^T$. α in this equation is the path length from the origin of the inertial frame to the mirror surface along the $\hat{\mathbf{z}}$ direction.

It is also useful to use Equation (1) to estimate the mirror angles from measurements of the command voltages.

$$\begin{bmatrix} \hat{\phi}^{FSM}_{Az.} \\ \hat{\phi}^{FSM}_{El.} \end{bmatrix} = (\mathbf{S^T S})^{-1} \mathbf{S^T} \cdot \mathbf{SF_{PZT}} \cdot \begin{bmatrix} V_1 - V_{bias} \\ V_2 - V_{bias} \\ V_3 - V_{bias} \end{bmatrix}. \quad (5)$$

Hysteresis and Dynamic Coupling— In this section, two experiments are described that are used to identify the input\output behavior of the fast steering mirrors. We are interested in both the static and dynamic behavior of the mounts. PZT hysteresis dominates the low frequency response of the mechanism. Characterizing this behavior allows us to predict the amount of piston motion seen by the path length control system and to determine how accurately we can expect to point the mirrors with an open loop scheme. Understanding the dynamic behavior of the mounts will tell us if any resonances limit the bandwidth of the closed loop control system.

The PZT hysteresis was characterized by measuring the linear displacement of the mirror surface using an HP interferometer. The interferometer provided 10 nanometer resolution over the 8.0 micron stroke of the PZT stack. A voltage signal generated from the step response of an underdamped second order system was applied to a single PZT stack, during which measurements of the stack displacement were made at 5 Hz. The results of this experiment are shown in

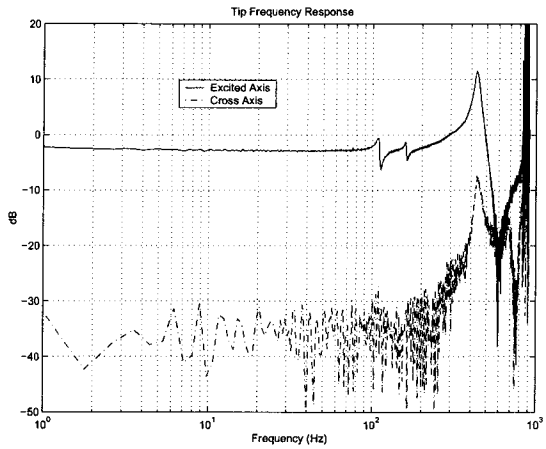

Figure 5. Mirror elevation (tip) frequency response. Both the excited axis and cross axis are shown.

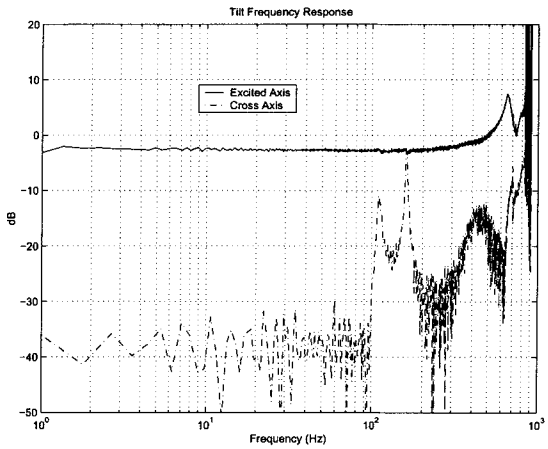

Figure 6. Mirror azimuth (tilt) frequency response. Both the excited axis and cross axis are shown.

Figure 3. Note the decreasing magnitude of the hysteresis loops and levelling off of the input\output behavior as the swing of the voltage signal decreases.

For purposes of control system analysis and design, a model was developed to predict the effect of hysteresis. In contrast to other approaches [2], [3] the model developed here attempts to characterize only the static nonlinear behavior of the PZT stack. The dynamic behavior of the PZT element is not relevant in this instance because the sample rates of the control loop are well below PZT resonances, which are typically on the order of several kHz. Our model uses a parallel connection of backlash elements (See Figure 4.) as basis functions for the hysteresis. Each backlash element has a unique deadband width and output gain which can be calculated from experimental data. The first hysteresis element in the parallel connection is assumed to have zero deadband width giving an exact linear input\output relationship. The remaining elements are used to model the nonlinear component of the hysteresis loop. To specify the output gains and deadband widths of each backlash element it is sufficient to use the voltage and displacement data from a full scale ramp input of the voltage command. The input (voltage)\output (displacement) curve can then be evaluated at n+1 predetermined input voltages which represent one half the deadband values of the backlash elements. Empirically, we have found that populating the portions of the hysteresis loop that have larger curvature with a higher density of deadband limits improves the performance of the model. Using this same set of points, the slope of the hysteresis curve between the deadband limits can be approximated with piecewise linear segments. Denoting the vector of local slopes as $\mathbf{s} = [\mathbf{s_0}\ \mathbf{s_1}\ \ldots\ \mathbf{s_n}]^{\mathbf{T}}$ with s_0 the low voltage slope and s_n the high voltage slope, the relationship between these slopes and the output gains of our model is given by,

$$\begin{bmatrix} s_0 \\ s_1 \\ \vdots \\ s_n \end{bmatrix} = \begin{bmatrix} 1 & 0 & \cdots & 0 \\ 1 & 1 & & \\ \vdots & & \ddots & \\ 1 & & \cdots & 1 \end{bmatrix} \begin{bmatrix} k_0 \\ k_1 \\ \vdots \\ k_n \end{bmatrix}. \tag{6}$$

With the slopes calculated from the piecewise linear segments, Equation (6) is easily inverted to find the output gains.

Overlayed on Figure 3 is the simulated output of the hysteresis model subject to the same input signal used on the PZT stack. We have found that a model with 13 parallel elements is sufficient to accurately reproduce the experimental results. The advantage of this particular model relative to others is that it is extremely fast numerically and does not require a small integration time step. This advantage is important when dealing with systems that have much larger time constants then the PZT dynamics, which is a common situation. The hysteresis model and Equation (4) were also successful at predicting the amount of piston motion seen experimentally.

To determine the dynamic behavior of the fast steering mirror, laser light from a He-Ne source was reflected from the mirror surface, through a 26.7X compressor and 200 mm lens onto a silicon based light sensitive position sensing device (OnTrak PSM with OT-301 amplifier.) with a calibrated scale factor of 2.0e-4 m/volt. The combined sensitivity of the optical arrangement was $2 \cdot 26.7 \cdot 200 \cdot (1/1000)$ m/rad. Azimuth and elevation chirp signals with an amplitude of ± 7.2 arc seconds were injected to the FSM and the output angular motion was recorded with the PSM. Equation (1) was used to calculate the necessary command voltages to the individual PZT stacks. Both the input PZT command voltages and output PSM signals were sampled at 12.8 kHz. The chirp signals swept from 0.1 Hz through 1.0 kHz.

The frequency response of the fast steering mirror mount is shown in Figures 5 and 6 for the elevation and azimuth cases respectively. Note that at low frequency some amplitude attenuation is visible which is due to hysteresis. At high frequency, we see that the mount axes become highly coupled and it is difficult to predict the behavior of the mount. Note that these resonances do not appear below 100 Hz. With the bandwidth limitations imposed by the 50 Hz frame rate these resonances should not present a stability problem for the control loops.

Air Path Disturbance Modelling

The disturbance environment in the FIT testbed is quite distinct from what can be expected in flight. In the laboratory, the effect of air path on the CCD measurements is the primary disturbance source, whereas vibrations, communication delays, and interspacecraft relative motion are likely to dominate the flight environment.

To characterize the effect of air path on the centroid measurements, full frame (40x40 pixels) camera data was logged for 60.0 seconds at the control loop sampling rate of 50 Hz. 7x7 pixel subwindows around both the right side fringe and pointing spots were used to calculate centroids. The centroids were calculated using a simple center of gravity algorithm,

$$\bar{x}_{c.g.} = \frac{\sum_{j=\bar{x}-3}^{\bar{x}+3}\sum_{i=\bar{y}-3}^{\bar{y}+3}(\mathbf{F}(i,j)-\mathbf{F}_{bias})\cdot j}{\sum_{i=\bar{y}-3}^{\bar{y}+3}\sum_{j=\bar{x}-3}^{\bar{x}+3}\mathbf{F}(i,j)-\mathbf{F}_{bias}},$$

$$\bar{y}_{c.g.} = \frac{\sum_{i=\bar{y}-3}^{\bar{y}+3}\sum_{j=\bar{x}-3}^{\bar{x}+3}(\mathbf{F}(i,j)-\mathbf{F}_{bias})\cdot i}{\sum_{i=\bar{y}-3}^{\bar{y}+3}\sum_{j=\bar{x}-3}^{\bar{x}+3}\mathbf{F}(i,j)-\mathbf{F}_{bias}}, \quad (7)$$

where $\bar{x}$ and $\bar{y}$ are the center of the subwindow in pixel coordinates, $\mathbf{F}(i,j)$ is the array of pixel values, and $\mathbf{F}_{bias}$ is used to represent the sum of CCD bias and dark current. Note, the centroid values as calculated are in global pixel coordinates. For control, the pointing centroids were converted to a local frame centered in the subwindow. The power spectral densities of these signals, minus their mean values, are shown in Figure 7. The shape of the curve in this figure suggests that a second order model of the following form is sufficient to capture the spectral content of the centroid data.

$$\bar{x}\,or\,\bar{y}_{c.g.}(s) = \underbrace{\frac{k}{b_1 s^2 + b_2 s + b_3}}_{G^{SF}(s)} w^{air}(s) \quad w^{air}(t) \in \mathcal{N}(0,1) \quad (8)$$

$w^{air}(t)$ in this equation is unit variance, Gaussian white noise. The parameters in this model were calculated based on a curve fit to the frequency domain data. This resulted

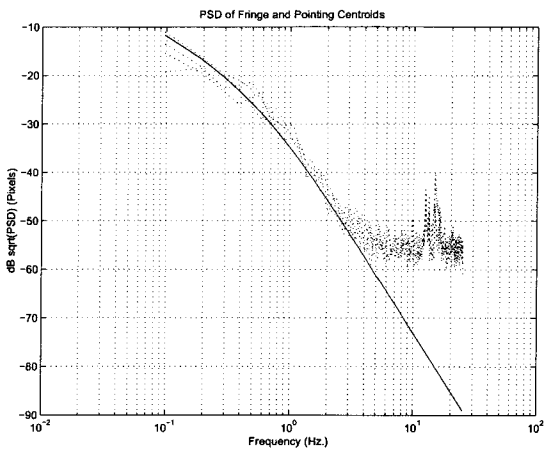

Figure 7. Power spectrum of camera centroid measurements. The experimental data set consists of X and Y centroid coordinates for both the fringe and pointing spots.

in the following transfer function.

$$G^{SF}(s) = \frac{0.45}{0.517s^2 + 2.5s + 1} \quad (9)$$

As shown in Figure 7 this model accurately fits the low frequency component of the air path PSD. The higher frequency component of the PSD was assumed to be attributed to pixel noise and was modelled as a pure white noise process, v^{pixel}, that is uncorrelated with the air path process. This speculation was verified through simulation of the centroiding Equations (7) with a Gaussian spot shape ($\sim$ 3.0 pixel diameter) subject to the same amount of pixel noise observed in the frame data (σ = 20 DN). The simulation resulted in the same amount of centroid noise, $\sigma_{v^{pixel}}$ = 0.01 pixels, as was seen in the experimental time series data. The transfer function in Equation (9) was converted to state space form $(\mathbf{A}_{SF}, \mathbf{B}_{SF}, \mathbf{C}_{SF}, 0)$ and discretized at 50 Hz for implementation in the simulation testbed. See [1] for details on the discretization procedure.

Ideally, the pointing and fringe spots for each aperture of the interferometer should be perfectly correlated with one another. In flight this should be the case for the current beam combiner design. In the laboratory, however, analysis of the frame data revealed significant discrepancies in the correlation of the two spots which will affect fringe visibility. In some cases, we have observed relative motion between the pointing and fringe spots on the order of $\sigma = 0.1$ pixels. Since the pointing spot is being used as a sensor for the fringe spot motion, any relative motion between the two spots cannot be corrected with control and directly adds to error in wavefront tilt. Given that it is possible for the relative motion to be on the order of one tenth of a pixel, the entire error budget can be consumed by the uncontrollable motion of the fringe spot.

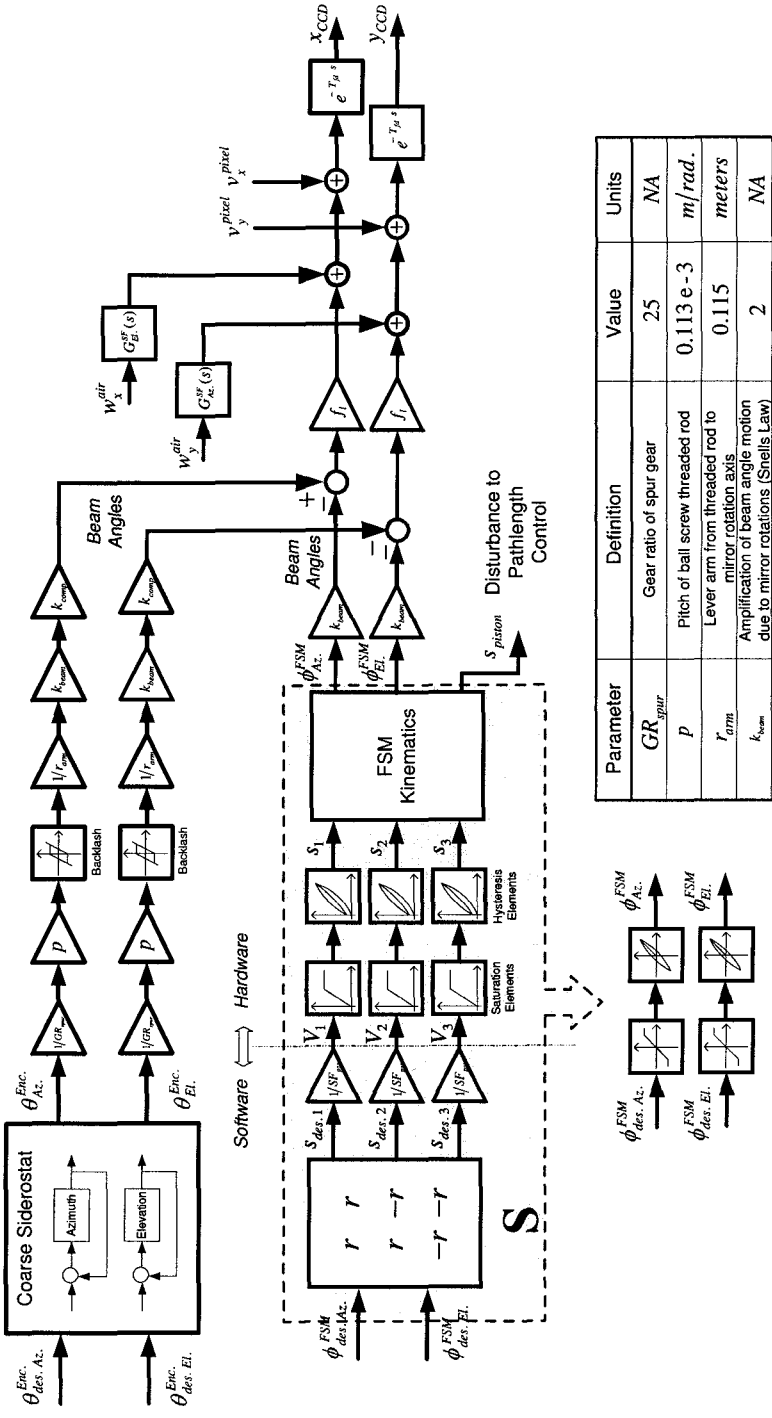

Parameter	Definition	Value	Units
GR_{spur}	Gear ratio of spur gear	25	*NA*
p	Pitch of ball screw threaded rod	0.113 e - 3	*m/rad.*
r_{arm}	Lever arm from threaded rod to mirror rotation axis	0.115	*meters*
k_{beam}	Amplification of beam angle motion due to mirror rotations (Snells Law)	2	*NA*
k_{comp}	Compressor amplification	4	*NA*
f_l	Effective focal length of camera sensor	0.457	*meters*
SF_{pzt}	PZT scale factor	8.0e - 7	*m/volt*
r	Half the separation distance of the PZT stacks	0.0225	*meters*
k_{BASIGA}	Coarse stage (siderostat) control gain	3227.0	*NA*
$\phi^{FSM}_{\max}$	Half the FSM deadzone width	1.772 e - 4	*rad.*
T_{fd}	Frame delay	0.035	*sec.*

Figure 8. Open loop model of the two stage FIT pointing system. The model includes backlash in the coarse siderostat and hysteresis in the vernier fast steering mirror. The correlated effect of air path on the camera measurements is modelled with shaping filters. Camera pixel noise is modelled by additive white noise. The delay block in the model is used to represent the time delay of 35 milliseconds in accessing measurements of the CCD frame.

The likely cause of the uncorrelated behavior between the fringe and pointing spots is the unique air paths traversed by the pointing and fringe starlight. Referring to Figure 2, two candidates come to mind that could explain the uncorrelated behavior of the spots. 1.) Before the parabolic mirror, the outer annulus of the compressed starlight beam is separated from the light used for the fringe spot and travels a unique path of about 0.6 meters along the focal length of the mirror. 2.) Another possibility is that the discrepancy is caused prior to the light entering the combiner when the aperture of the starlight is larger. Here, since the cross section is large ($\sim$ 6.0 inche diameter), the scale of the air path distortions might be small enough to distort the fringe or pointing light separately.

The overall model of the coarse and fine pointing system is summarized in Figure 8. Note the shaping filters and additive noise at the outputs which represent the effect of the air path disturbance and pixel noise, respectively, on the centroid measurements. Also included in the model is a delay of 35 milliseconds associated with clocking out the frame and passing it across a VME bus to the testbed computer. This is a significant amount of delay relative to the sampling period of 20 milliseconds and will limit the bandwidth of the closed loop system as will be shown in the next section.

3. Coarse/Vernier Controller Design

Because the FIT pointing system has dual stage actuation, one of the challenges is to coordinate the control of both actuators in a manner that takes advantage of the unique characteristics of each steering mirror. The siderostat is a low bandwidth, large range of motion actuator. The FSM, on the other hand, is a high bandwidth mechanism, but has a limited range of motion ($\pm$36.5 arc seconds or $\pm$6.75 pixels at the camera.). The approach taken to coordinate the motion of the two actuators is to correct DC offsets in the error signal with the coarse siderostat and use the fast steering mirror to reject the high frequency, low amplitude, air path disturbance. This will keep the fast steering mirror near the center of its range of motion to preserve the maximum amount of articulation range, and simultaneously allow for adding the maximum amount of bias for alignment purposes [4].

The desired behavior of the pointing system can be achieved if an integrator is added to the coarse loop and the vernier loop is constrained to have a constant gain at low frequency (See Figure 9.). This will cause persistent error signals to be integrated out by the siderostat, while high frequency components of the error signal are attenuated with the fast steering mirror.

Note in Figure 7 that most of the power of air path disturbance is below 2.0 Hz and that the relatively low sampling rate of the camera, 50 Hz, restricts the amount of disturbance rejection we can expect to achieve. Nevertheless,

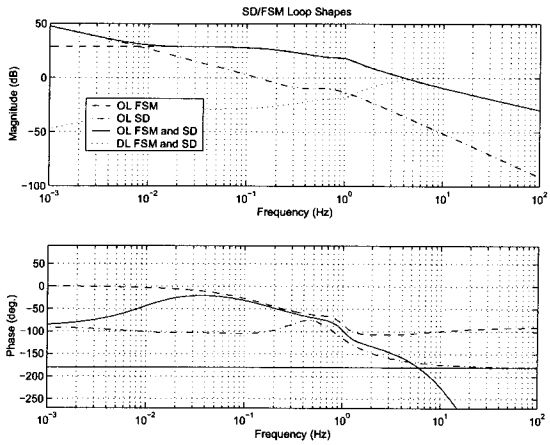

Figure 9. Coarse and vernier loop shapes. Note the significant degradation in phase resulting from the frame delay limiting the bandwidth to $\sim 5.0Hz$..

control does offer the functionality to move the pointing and fringe spots within the focal plane of the camera which is critical for accurately overlapping the right and left fringe spots. Moreover, stellar acquisition mandates coordination between the coarse and fine steering mirrors.

LQG/LTR Vernier Design

Combining the dynamics of the disturbance process with those of the FSM we arrive at the following state space description of a single axis for the vernier loop,

$$\begin{bmatrix}\dot{\mathbf{x}}_{SF}\\ \dot{\mathbf{x}}_P\end{bmatrix} = \underbrace{\begin{bmatrix}\mathbf{A}_{SF} & \mathbf{0}\\ \mathbf{0} & \mathbf{A}_P\end{bmatrix}}_{\mathbf{A}^o}\begin{bmatrix}\mathbf{x}_{SF}\\ \mathbf{x}_P\end{bmatrix} + \underbrace{\begin{bmatrix}\mathbf{B}_{SF} & 0\\ 0 & \mathbf{B}_P\end{bmatrix}}_{\mathbf{B}_w}\begin{bmatrix}w^{air}\\ w_\phi\end{bmatrix} + \underbrace{\begin{bmatrix}0\\ \mathbf{B}_P\end{bmatrix}}_{\mathbf{B}^o}\phi_{des.} \tag{10}$$

$$y = \underbrace{\begin{bmatrix}\mathbf{C}_{SF} & \mathbf{C}_P\end{bmatrix}}_{\mathbf{C}^o}\begin{bmatrix}\mathbf{x}_{SF}\\ \mathbf{x}_P\end{bmatrix} + v^{pixel} \tag{11}$$

where the measurements, y, are of the centroid position in units of meters. w_ϕ is used to represent the pointing uncertainty of the FSM caused by hysteresis and $\phi_{des.}$ is the control input to the FSM plant. Note, from Figure 8, that the FSM plant is modelled by a static system with no memory, excluding the hysteresis memory, but that with the inclusion of $(\mathbf{A}_P, \mathbf{B}_P, \mathbf{C}_P)$, we have allowed for the possibility of augmenting the FSM system with some desirable dynamics which is allowed in the LQG\LTR design procedure. In this particular case, we augment the FSM system with the following dynamics to introduce the desired shape to the vernier loop.

$$G_{augm}(s) = \frac{\omega_n^2}{s^2+2\zeta\omega_n s+\omega_n^2}\frac{s^2+2\zeta_z^{notch}\omega_n^{notch}s+\omega_n^{notch^2}}{s^2+2\zeta_p^{notch}\omega_n^{notch}s+\omega_n^{notch^2}} \tag{12}$$

The natural frequency, ω_n, is set to establish the breakdown frequency of the FSM loop. The notch filter is added with $\zeta_z^{notch} > \zeta_p^{notch}$, to increase the gain near the crossover for enhanced disturbance rejection in this region. The matrices $(\mathbf{A}_P, \mathbf{B}_P, \mathbf{C}_P)$, in Equations (10)-(11) are derived from the state space realization of Equation (12).

The fictitious Kalman filter was used to obtain the target feedback loop (TFL). In this formulation the measurement noise term is adjusted for loop shaping. The Kalman filter is used to design the TFL because of its superior robustness and disturbance rejection properties. As will be shown, the Kalman filter shapes the open loop frequency response near the crossover in such a way that disturbances are not amplified. In this application this property is particularly important because the air path disturbance is uncomfortably close to the open loop crossover. The target feedback loop,

$$G_{TFL}(s) = \mathbf{C}^o(s\,\mathbf{I} - \mathbf{A}^o)^{-1}\mathbf{F} \tag{13}$$

is obtained from solving the Ricatti equation associated with the infinite horizon Kalman filter:

$$\mathbf{F} = \mathbf{M}\mathbf{C}^{oT}V^{-1}$$
$$\mathbf{A}^o\mathbf{M} + \mathbf{M}\mathbf{A}^{oT} - \mathbf{M}\mathbf{C}^{oT}V^{-1}\mathbf{C}^o\mathbf{M} + \mathbf{B}_w\mathbf{W}\mathbf{B}_w^T = \mathbf{0},$$
$$\mathbf{M} > \mathbf{0}. \tag{14}$$

In this Equation $\mathbf{W}$ represents the covariance of the random input terms in Equation (10),

$$\mathbf{W} = \begin{bmatrix} \sigma^2_{w^{air}} & 0 \\ 0 & \sigma^2_{w_\phi} \end{bmatrix}. \tag{15}$$

Recall that $\sigma_{w^{air}} = 1.0$. σ_{w_ϕ} is used to capture the uncertainty in pointing the FSM associated with PZT hysteresis. Although the pointing uncertainty is not a stochastic quantity we can represent it as such for the purposes of loop shaping. V in Equation (14) represents measurement uncertainty and is used in this context to place the TFL cross over frequency. Smaller V corresponds to higher cross over frequency. V was set to maximize the bandwidth of the vernier loop subject to the constraint that the phase and gain margins of the following loop transfer gain remain stable.

$$\exp(-T_{fd}s)\left(C^{SD}(s) + C^{FSM}(s)\right) \tag{16}$$

Note in Figure 9 that the loop phase lag increases dramatically due to the effect of frame delay in the camera measurements. This delay is the limiting factor in achieving the widest possible bandwidth.

The loop transfer recovery (LTR) is achieved using a "cheap" LQ formulation, such that the product of an LQG based compensator,

$$C_{LQG}(s) = \mathbf{K}(s\,\mathbf{I} - \mathbf{A}^o + \mathbf{F}\mathbf{C}^o + \mathbf{B}^o\mathbf{K})^{-1}\mathbf{F}, \tag{17}$$

where,

$$\mathbf{K} = R^{-1}\mathbf{B}^{oT}\mathbf{P}$$
$$\mathbf{A}^{oT}\mathbf{P} + \mathbf{P}\mathbf{A}^o - \mathbf{P}\mathbf{B}^{oT}R^{-1}\mathbf{B}^o\mathbf{P} + \mathbf{C}^{oT}\mathbf{C}^o = \mathbf{0},$$
$$\mathbf{P} > \mathbf{0}. \tag{18}$$

with the nominal plant,

$$G^o(s) = \mathbf{C}^o(s\,\mathbf{I} - \mathbf{A}^o)^{-1}\mathbf{B}^o, \tag{19}$$

will approach (recover) the TFL, $G_{TFL}(s)$, as $R \to 0$ [1].

Following the design procedure outlined above, the loop recovery was achieved by setting $R = 0.5e-9$ and solving the second Riccati Equation (18). This resulted in the following compensator for the vernier loop,

$$C^{FSM}(s) = C_{LQG}(s)G^o(s) = \frac{18.3(s+25.0)(s+4.5)}{(s+15.6)(s+4.4)(s+1.2)}$$
$$\frac{(s+0.5)(s^2+5.5s+37.2)(s^2+5.98s+39.5)}{(s+0.44)(s^2+5.9s+39.1)(s^2+3.8s+39.9)}, \tag{20}$$

where the order has been reduced by two to account for the elimination of two unnecessary high frequency poles that result from the finite recovery of the LTR procedure.

Coarse Siderostat Design

The bandwidth of the coarse siderostat loop is limited by backlash in the drive mechanism [1]. Empirically it was determined that a bandwidth much beyond a tenth of a hertz resulted in oscillations within the loop. The reason for this can be explained in terms of a describing function analysis [1]. The loop shape for the siderostat is shown in Figure 9. Note the larger slope at low frequency relative to the vernier loop and the lower bandwidth. Also shown in Figure 9 is the amount of disturbance attenuation achieved by the combination of both the coarse and vernier loops. At 1.0 Hz., for example, the influence of the air path disturbance on the error signal is attenuated by a factor of 10.

Note in Figure 10 that a prefilter has been added to the control system to reduce the possibility of saturating the FSM when large amplitude commands are given. The prefilter is second order with a 1.0 second time constant and critically damped poles.

4. Simulation and Experimental Results

Figures 11 and 12 are included to explain the operation and demonstrate the performance of the pointing system. Figure 11 demonstrates motion of the fast steering mirror and siderostat for a step change in the elevation beam angle command. As the new command is issued at $t = 2.0$ seconds, the FSM reacts first to cancel the error. As the siderostat responds to integrate out the residual error not corrected for by the FSM, the FSM signals return to having zero bias. The high frequency seen in the FSM commands represent the reaction of this loop to the air path disturbance. Note the siderostat commands do not react to the air path disturbance because the gain of the siderostat loop is small at these high frequencies. Note also that even though

[1] R represents the penalty on the control input in the formulation of the performance index in LQ theory. Hence the terminology "cheap" control.

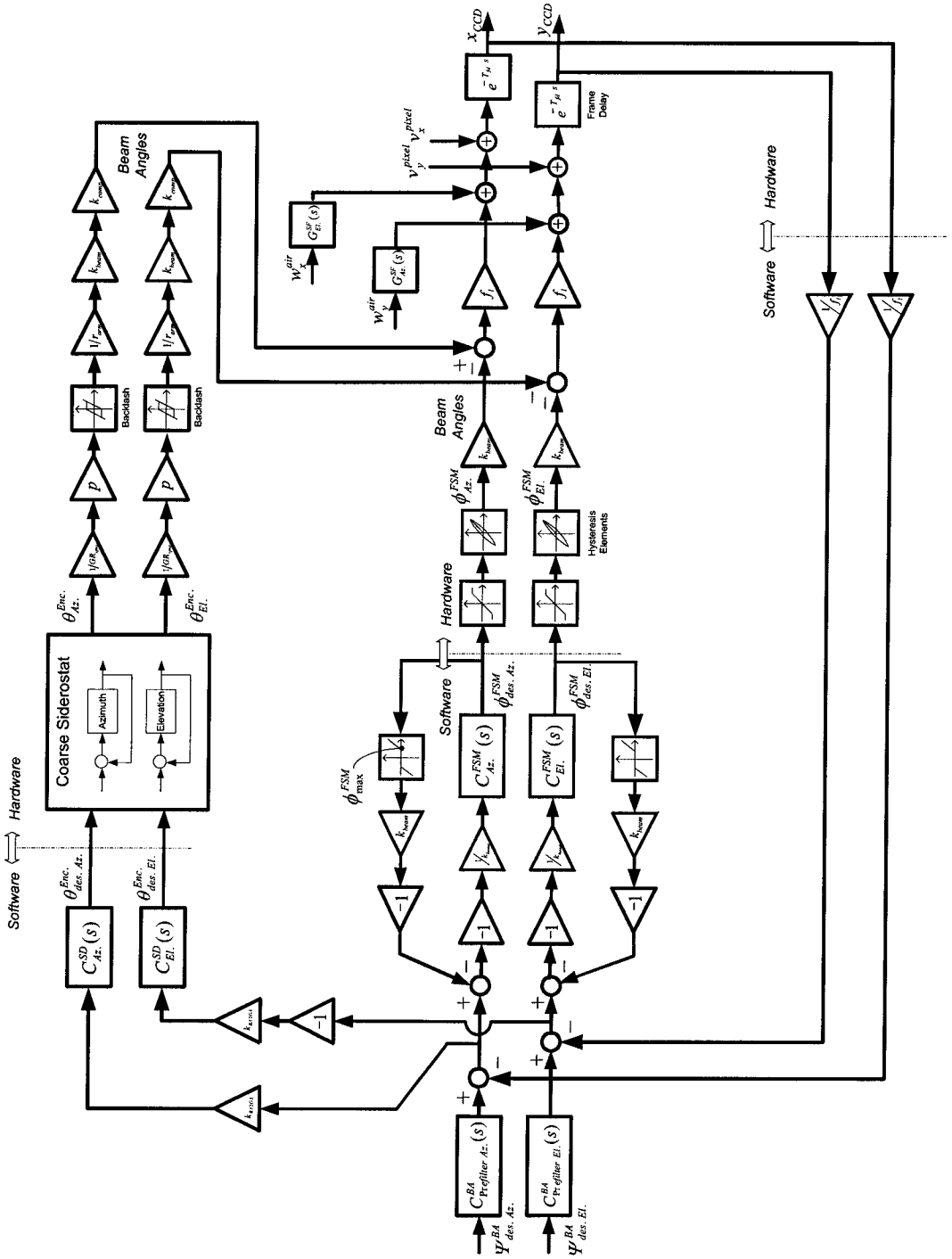

Figure 10. Block diagram of dual stage closed loop pointing system. The controller has a parallel architecture, with nonlinear feedback about the vernier loop.

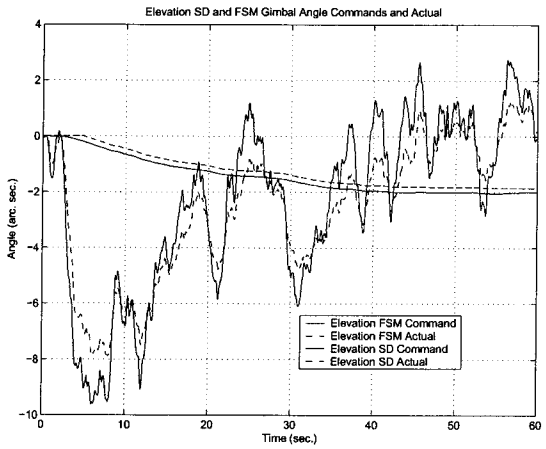

Figure 11. Simulated steering mirror commands for a step input change in the commanded beam angle.

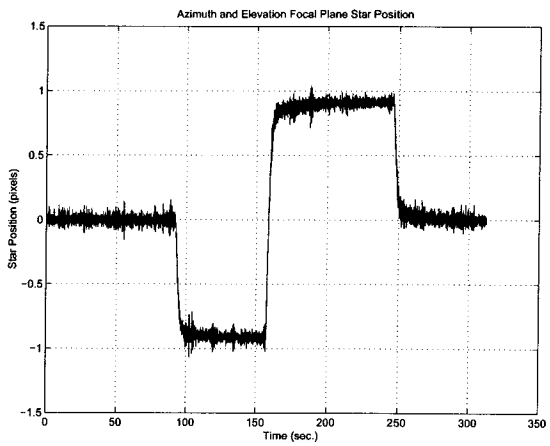

Figure 12. Experimental azimuth and elevation star position as calculated using a center of mass algorithm.

the repositioning of the star spot is achieved in a few seconds, the system takes several tens of seconds to settle. The true mirror positions are also shown in Figure 11. In the case of the siderostat, the true position is different from the command because of backlash. For the FSM, the true position is different because of hysteresis in the PZT stacks.

Figure 12 demonstrates real time star position data logged using the FIT testbed. In this figure, the star position is jogged by $\sim \pm 1.0$ pixels. The steady state RMS pointing error is $1/35$ of a pixel, more then three times better then the pointing requirement based on fringe visibility. Note the smooth transitions of the star position in this figure caused by prefiltering the step changes in commanded beam angle.

Nonlinear Operation

During stellar acquisition it is anticipated that the spiral search [1] will issue commands that will saturate the FSM. To prevent undesirable effects of the saturation, nonlinear feedback elements have been added to the vernier loop (See Figure 10.). These deadzone elements provide additional feedback once the commands to the actual mirrors have saturated, making the fast steering mirror appear to the compensator as a system without saturation. This feedback, of course, does not prevent the saturation, but does prevent the compensator from reacting to error signals large enough to cause saturation. This improves the transient response of the vernier stage as it comes out of saturation.

In acquisition mode, by definition, measurements of the star position from the camera are not available. The impact point of the star spot must be estimated in this mode using measurements of the siderostat encoders and voltage commands to the FSM. Even though there is a certain amount of uncertainty in these measurements because of siderostat backlash and PZT hysteresis, they should be accurate enough for acquisition purposes.

5. Conclusions/Future Work

In this paper the stellar pointing system for the FIT testbed has been described. The performance of the pointing system has been shown to exceed the requirements by a factor of three. Delay in measuring the camera frame was determined to be the fundamental limit in achieving higher bandwidth. For the flight design, delays are likely to remain the primary factor limiting the bandwidth. Even though the frame rate is increased to 500 Hz. in the flight design, the bandwidth requirement is also increased. We have also seen that the effect of air path on the angular metrology is significant and its effect must be planned for during integration and test of the flight system. To compensate for its influence on the relative motion between the pointing and fringe spots, evacuated pipes with windows may have to be installed.

This paper has focused on the right side stellar loop. The left side stellar loop is slightly more complex because of coupling with the interspacecraft metrology loop. To eliminate this coupling, the metrology sensor measurements and or the left combiner siderostat encoder measurements should be used as a feedforward signal to the left stellar loop. It is anticipated that a full discussion of the left side loops will be published in a future paper.

The hysteresis model developed in this paper has potentially wide applicability because of its simplicity and ease of use. In addition to the field of interferometry, any application using actuators and sensors with this type of nonlinearity could find utility in this type of model. Strain gauges, pressure sensors, and magnetic sensors are just a few of the possible areas that come to mind.

The design process of the dual stage system was decoupled in that the coarse and fine stage loops were designed separately and later tested for overall stability. Other design approaches such as FSLQ [5] could have been used that

unify the design process by treating both stages in a single performance index. These alternate approaches offer simplicity at the cost of less flexibility in the design. Custom designs, based on detailed models, offer the possibility of optimizing performance. Furthermore, detailed models, such as the one developed here, offer the ability to design and predict performance of a control algorithm before it is actually implemented in the laboratory.

REFERENCES

[1] J. Shields, S. Sirlin, and M. Wette, "Metrology sensor characterization and pointing control for the formation interferometer testbed (FIT)," Big Sky, Montana, March 2002, IEEE Aerospace Conference, IEEE.

[2] M. Goldfarb and N. Celanovic, "Modeling piezoelectric stack actuators for control of micromanipulation," *IEEE Control Systems*, pp. 69–79, June 1997.

[3] P. R. Dahl and R. Wilder, "Math model of hysteresis in piezo-electric actuators for precision pointing systems," 1985, pp. 61–88, AAS.

[4] M. Wette, "A linear covariance technique for analyzing a closed-loop alignment problem," DRAFT, 2001.

[5] M. Tomizuka, "Class notes: Advanced control systems II, ME233," 1994.

[6] B. J. Lurie and P. J. Enright, *Classical Feedback Control With MATLAB*, Marcel Dekker Inc., New York, 2000.

[7] M. Born and E. Wolf, *Principles of Optics*, Cambridge University Press, 1999.

[8] T. C. Chiu, C. Kempf, W. H. Yao, and M. Tomizuka, "Compensation for repeatable and non-repeatable tracking errors in disk file systems," Tokyo, August 1993, International Conference on Advanced Mechatronics.

[9] B. D. O. Anderson and J. B. Moore, *Optimal Control Linear Quadratic Methods*, Prentice Hall Information and System Sciences Series. Prentice-Hall, New Jersey, 1990.

[10] R. K. Tyson, *Principles of Adaptive Optics*, Academic Press, 1991.

[11] M. Berthold and D. J. Hand, *Intelligent Data Analysis*, Springer-Verlag, 1999.

[12] J. R. Ragazzini and G. F. Franklin, *Sampled-Data Control Systems*, McGraw-Hill, 1958.

[13] O. Bottema and B. Roth, *Theoretical Kinematics*, Dover, 1979.

[14] B. W. Kernighan and D. M. Ritchie, *The C Programming Language*, Prentice-Hall, 1988.

[15] R. M. Murray, Z. Li, and S. S. Sastry, *A Mathematical Introduction to Robotic Manipulation*, CRC Press, 1994.

[16] J. J. E. Slotine and W. Li, *Applied Nonlinear Control*, Prentice-Hall, 1991.

[17] L. Ljung, *System Identification Theory for the User*, Prentice-Hall, 1987.

[18] B. J. Lurie, J. J. Hench, A. Ahmed, and F. Y. Hadaegh, "Nonlinear control of the optical delay line pathlength," Orlando, Florida, April 1999, SPIE, vol. 3692, pp. 139–149.

[19] D. S. Bayard, "Statistical plant set estimation using schroeder-phased multisinusoidal input design," *Applied Mathematics and Computation*, vol. 58, pp. 169–198, 1993.

[20] G. W. Neat, J. W. Melody, and B. J. Lurie, "Vibration attenuation approach for spaceborne optical interferometers," *IEEE Transactions on Control Systems Technology*, vol. 6, no. 6, pp. 689–700, November 1998.

Joel Shields *is a member of the Guidance and Control Analysis Group at the Jet Propulsion Laboratory. He received his B.S. degree in Applied Mechanics from U.C. San Diego in 1990 and his M.S. and Ph.D. degrees in Control Systems from U.C. Berkeley in 1993 and 1997, respectively. His dissertation research was on control of exercise machines. He developed three exercise machine prototypes that use feedback from the user to actively change the workout based on a given performance criteria. He is the holder of a patent based on this work. Upon graduation, Dr. Shields worked as a consultant before joining the technical staff at JPL. Dr. Shields has extensive experience in design of mechatronic systems, system identification, adaptive control, precision servo control, and real time applications of control systems. Currently, he is working on pointing control for space based interferometry.*

Samuel Sirlin *has a Ph.D. in Mechanical Engineering from Columbia University (1983). From October 1983 to the present he has been Member of the Technical Staff of JPL. His background and expertise covers the areas of dynamics and simulation, controls and estimation. During his time at JPL he has worked on a number of research and flight projects including Galileo, precision pointing, Ulysses, Control Structure Interaction research, Mars Pathfinder (launch vehicle stability analysis, attitude control design, landing system), inflatable antenna analysis and control, Modelling and Analysis for Controlled*

Optical Systems (MACOS), Integrated Modelling of Optical Systems (IMOS), Deep Space 1 (DS1), the DS1 rescue, Starlight, and Mars Exploratory Rover (MER). He has published 26 conference papers and 4 journal articles.

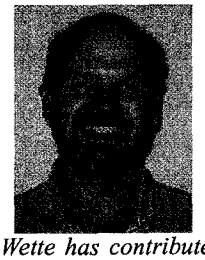

Matt Wette *has a Ph.D. in Electrical and Computer Engineering from UCSB (1988). Currently he is a Senior Engineer at the Jet Propulsion Laboratory in the Guidance and Control Analysis Group. His interests are in control system design, real-time systems, and discrete event control. Dr. Wette has contributed to several projects in the development of real-time simulation testbeds. He is currently working on interferometer control for the StarLight project.*